Dynamic modelling of a compressed heat energy storage system integrated with a cascaded phase change materials thermal energy storage

Tafone, Alessio; Pili, Roberto; Pihl Andersen, Martin; Romagnoli, Alessandro

Published in:
Applied Thermal Engineering

Link to article, DOI:
10.1016/j.applthermaleng.2023.120256

Publication date:
2023

Document Version
Peer reviewed version

Journal Pre-proofs

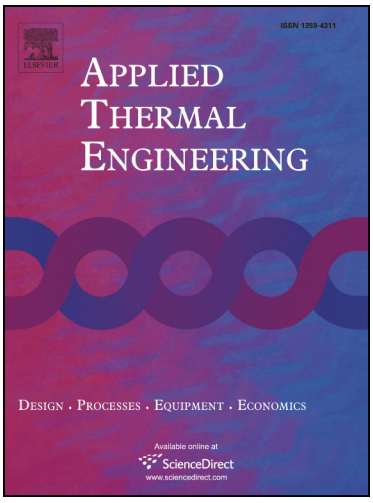

Research Paper

Dynamic modelling of a compressed heat energy storage system integrated with a cascaded phase change materials thermal energy storage

Alessio Tafone, Roberto Pili, Martin Pihl Andersen, Alessandro Romagnoli

PII: S1359-4311(23)00285-5
DOI: https://doi.org/10.1016/j.applthermaleng.2023.120256
Reference: ATE 120256

To appear in: *Applied Thermal Engineering*

Received Date: 14 October 2022
Revised Date: 26 December 2022
Accepted Date: 16 February 2023

Please cite this article as: A. Tafone, R. Pili, M. Pihl Andersen, A. Romagnoli, Dynamic modelling of a compressed heat energy storage system integrated with a cascaded phase change materials thermal energy storage, *Applied Thermal Engineering* (2023), doi: https://doi.org/10.1016/j.applthermaleng.2023.120256

Dynamic modelling of a compressed heat energy storage system integrated with a cascaded phase change materials thermal energy storage

Alessio Tafone[a*], Roberto Pili[b], Martin Pihl Andersen[b], Alessandro Romagnoli[c†]

[a] *Surbana Jurong – NTU Corporate Lab, Nanyang Technological University, Singapore, Singapore*
[b] *Department of Civil and Mechanical Engineering, Section of Thermal Energy, Technical University of Denmark, Lyngby, Denmark*
[c] *School of Mechanical and Aerospace Engineering, Nanyang Technological University, Singapore*

Abstract

Carnot batteries represent an emerging thermo-mechanical energy storage technology based on the conversion of surplus electricity into medium-low temperature heat, and subsequent conversion of the heat into electricity. A promising Carnot battery's configuration is the Compressed Heat Energy Storage (CHEST) that combines a high-temperature heat pump (charge phase), an Organic Rankine Cycle (discharge phase) and a thermal energy storage (TES) system. As of now, all the literature studies on CHEST were designed to store the thermal energy into a cascaded TES combining a pressurized water storage for the sensible section and latent heat material for the evaporation and condensation sections. The objective of the present work is to numerically investigate a novel configuration of the TES system utilizing a cascade of multiple phase change materials (PCMs) in place of the cascade of sensible heat and phase change materials presented in literature, aiming to enhance both the energy density and the round trip efficiency of the system. The comparative technical analysis has been carried out by developing for the first time a dynamic numerical model of the CHEST system. Indeed, while the current literature studies on CHEST are only focused on preliminary analyses to define the general thermodynamic potential and to identify the limits of the overall system, this paper overcomes this gap and presents a detailed dynamic analysis of the CHEST with focus on TES modelling. Notably, the authors developed a plant model in MATLAB that blends together algebraic and differential sub-models detailing the transient behaviour of the CHEST system. The results are of interest for academia and industry and contribute significantly to the development of a more efficient CHEST system. Indeed, by enhancing the thermal buffer effect typical of PCM media and the TES operational time, the cascaded TES augments both the COP of the high-temperature heat pump (4.13 vs 3.79) and the electric efficiency of the ORC (11.69 % vs 11.31 %). As a result, the novel CHEST system based on cascaded PCMs is capable to achieve a round trip efficiency of 47.6 % and an energy density of 6.9 kWh_e/m^3, simultaneously increasing the respective values of the state-of-the-art solution by 13 % and 100 %, respectively.

Keywords: CHEST, PTES, Carnot battery, Heat pump, Organic Rankine cycle, Thermal energy storage, Phase change material.

* Corresponding authors. E-mail addresses: alessio.tafone@ntu.edu.sg (Alessio Tafone), a.romagnoli@ ntu.edu.sg (Alessandro Romagnoli).

Nomenclature

a_s	Shape Factor [m_2/m^3]	HP	Heat Pump
Bi	Biot Number [-]	HTF	Heat Transfer Fluid
C	Storage Media Specific Cost [$/kg]	HTHP	High Temperature Heat Pump
c_p	Specific heat capacity [kJ/kg K]	ORC	Organic Rankine Cycle
d	Particle diameter [m]	PCM	Phase Change Material
D	TES internal diameter [m]	RT	Round-Trip
k	Thermal conductivity [W/m K]	SH	Sensible heat material
h	Heat transfer coefficient [W/m^2 K]	TES	Thermal Energy Storage
H	TES height [m]	WHR	Waste Heat Recovery
$\dot{m}$	Mass flow rate [kg/s]	*Greek Symbols*	
L	Latent heat [kJ/kg]	η	Efficiency
Nu	Nusselt number [-]	ε	HGCS porosity [-]
Pr	Prandtl Number [-]	ρ	Density [kg/m^3]
Re	Reynolds Number [-]	φ	Energy density [kWh_e/m^3]
T	Temperature [ºC]	μ	Dynamic viscosity [Pa s]
T_m	Phase change temperature [ºC]	*Subscripts*	
U	Overall heat transfer coefficient [W/m^2K]	amb	ambient
Acronyms		ch	charge
CHEST	Compressed Heat Energy Storage	d	discharge
EES	Electrical Energy Storage	e	electric
HE	Heat Engine		

1. Introduction

The window of opportunity for a sustainable and net zero future is dramatically about to close. Indeed, according to IRENA [1] and IEA [2], to achieve the Paris Agreement goals and halt the pace of climate change by transforming the global energy landscape, a fast-paced pathway to a net zero future needs to be quickly undertaken. This transformation not only requires a rapid integration of renewables throughout all kinds of energy use, but also a scaling up of technologies, such as electrical energy storage systems (EESs), to help addressing the hour to hour variability of renewable energy systems, a critical challenge for grid balance and security [3]. EESs operating on a timescale of hours and performing their services at power ratings from MW_e to GW_e are important for the large-scale integration of fluctuating renewable power sources with limited regulation capability [4]. Among the grid-scale EESs, thermo-mechanical energy storage systems, known in literature also as Carnot batteries, have the lowest average technology readiness level (TRL), even though they are gaining momentum in literature. For this reason, despite the considerable interest in the last decades shown by the significant amount of research currently being carried out, the actual potential of Carnot batteries is still unclear. In addition, several pilot plants or pre-commercial demonstrators have been developed and successfully commissioned [5,6], or are currently being developed [7], to demonstrate the promising theoretical outcomes which were recently derived in literature.

The Compressed Heat Energy Storage (CHEST) system is a specific Carnot battery system, belonging to the Pumped Thermal Energy Storage (PTES) category [8], that nowadays is gaining significant momentum and interest among other Carnot batteries technologies such as Liquid Air Energy Storage (LAES) [5], Compressed Air Energy Storage (CAES) [9] and Rankine or Brayton heat engines [10]. Based on mature components such as heat pumps, Organic Rankine cycle (ORC) units and thermal energy storage, CHEST is a medium-long term thermo-mechanical based process, with one of the highest specific energy among PTES variants (40-100 kWh/m^3), suitable for mid-to-large scale applications (10-150 MW/ 80-7200 MWh) [9], without geographical constraints and environmentally safe. The CHEST system operation can be divided into three phases (Fig. 1): charging, storing, and discharging. During the charge phase, a high temperature heat pump (HTHP) makes use of electrical energy to compress a vapour organic fluid, produced by low temperature heat source. The fluid is then condensed and subcooled by transferring thermal energy to the thermal energy storage (TES), i.e., a cascade of sensible heat material (pressurized water) and phase change material (PCM). A conventional ORC unit is then operated during the discharge phase by utilizing the thermal energy stored in the TES to drive a turbine, thus feeding the electrical energy back into the grid. Due to its thermo-mechanical nature, the system can also provide thermal energy for a potential district heating application [11]. Under the CHESTER project's umbrella [12] a first-of-its-kind pilot/laboratory plant is expected to be built and presumably be operative in 2023 to be validated and integrated in a relevant environment including smart district heating. Among the thermal devices mentioned, the TES plays a key role in order to guarantee a reasonably high CHEST efficiency (>50 % [11]). Steinmann et al. [13] theoretically investigated the techno-economical feasibility of different CHEST configurations using various combinations of heat pumps, heat engines, thermal energy storages and working fluids. The authors highlighted the paramount influence of the engines' isentropic efficiencies on the round trip efficiency of the system that is stronger for systems based on Brayton thermodynamic cycles than for the ones based on Rankine thermodynamic cycles. Similar outcomes were presented by Roskosch et al. [14] that carried out a technical analysis on the CHEST system highlighting the main general thermodynamic potentials and limitations. The results showed that the system achieved round trip efficiencies in the range of 37-56 % only when the main components are assumed to be ideally operated in isentropic conditions. In order to formulate a simple empirical correlation to predict the round trip efficiency of the CHEST system, Thess [15] developed a thermodynamic model as a function of the TES temperature at the point of maximum power output. The formula predicted that for TES temperatures higher than 400 ºC, CHEST system achieved higher round trip efficiency than CAES. Jockenhöfer et al. [16] carried out a technical investigation on a fully heat integrated subcritical CHEST proposing a cascaded sensible-latent heat TES (SH-PCM) combining a pressurized water storage for the sensible part and a latent heat storage (eutectic mixture of potassium nitrate and lithium nitrate with T_{melt} = 133 ºC) for the phase change zones. If a heat source of 100 °C and a heat sink of 15 °C are available, the system can deliver a round trip efficiency as high as 125 %. Notably, it has been concluded that the further enhancement of the cascade concept through PCM utilization could be a critical key to technical success of the CHEST system. Aiming to develop a dynamic model of the CHEST coupled with a 26 MW_e wind farm located in Spain, Sánchez-Canales et al. [17] carried out a techno-economic analysis of the case scenario. The results showed that, with a round trip efficiency above 90 %, the CHEST is an economically viable energy storage system only when its capital cost (CAPEX) ranges between 235 and 765 k$/$MW_e$. It is worth noting that, despite the work claimed a fully dynamic approach for the whole plant, the TES is modeled with a simple quasi-steady state approach and once again the cascaded configuration SH-PCM is proposed in order to minimize the entropy generation during the heat exchange processes. Adopting a similar CHEST cycle architecture and steady-state approach, Hassan et al. [18] performed a thermodynamic analysis of a 1 MW_e CHEST system, assessing the effect of different refrigerants and cycle configurations for an extensive range of heat source and heat sink temperatures. R1233zd(E) and butene were selected as the best working fluids for HTHP and the ORC, respectively, assuming a system maximum temperature as high as 133 ºC. Instead, for a system adopting the same working fluids for both charge and discharge processes, the choice would fall either on R-1233zd(E) or R-1234ze(Z). The former working fluid has been selected as the best candidate by the same research group [19] for a high-temperature heat pump prototype and a model utilized for the development

of the characteristic performance maps of the device. The results highlighted that, to obtain reasonable performance values of the COP (>4), the heat source temperature at the inlet of the high-temperature heat pump should be higher than 60 ºC. Based on the model developed by Sánchez-Canales et al. [17], Trebilcock et al. [20] presented the design and different operation modes of a CHEST system. By utilizing the same steady-state approach common to other works, the authors confirmed the potential of the system achieving round trip efficiency values higher than 100 % when using waste heat/cold sources available. Aiming at the development of CHEST for smart district heating applications, the potential of CHEST operating as a multi-energy system, concurrently fulfilling electricity and heat demands, has been explored by Steinman et al. [21]. Using butene as main working fluid for both charge and discharge processes and the sensible heat and latent heat cascade approach for the TES, the CHEST system has been proposed to operate under six scenarios based on different combination of heat source and heat sink temperatures.

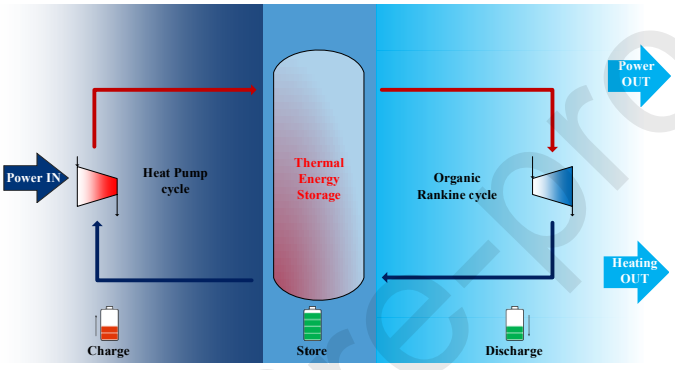

Fig. 1. CHEST block diagram process.

As extensively described in this section, although all the literature studies mentioned above highlighted the paramount importance of the thermal energy storage system, none of the works presented delved into an exhaustive technical analysis clearly identifying how the CHEST system performance is impacted by the dynamic performance of the TES. Indeed, thermodynamic analysis considering only steady-state approach, as insofar available in literature, are likely to 1) not capture the operational off-design conditions of the CHEST system and 2) provide an incorrect picture of the CHEST performance capabilities, mostly overestimating the round trip efficiency. Furthermore, although only highlighted by Jockenhöfer et al. [16], the potential to further enhance the cascade approach of the thermal energy storage has never been investigated in literature.

In this context, the present work aims to overcome these research gaps in the literature and goes a step further, introducing the following novelties: 1) a dynamic approach to fully assess the TES influence on the CHEST round trip efficiency 2) a novel TES configuration based on cascaded PCMs aiming to increase the energy density and the round trip efficiency of the CHEST system. By overcoming the limitations presented in literature and proposing a new modeling approach and a new architecture for the CHEST, the present work aims to demonstrate how: 1) the dynamic behaviour of the system must be properly accounted for when evaluating the thermodynamic performance of the system 2) the thermal energy storage cascaded concept can be further enhanced to promote a higher efficiency solution.

2. System description

The state-of-the-art architecture of the CHEST system proposed in literature is shown in Fig. 2 and represents the baseline case scenario. The system consists of three main components (a HTHP, a high-temperature TES and an ORC system) and operates as follows. The charge phase is driven by excess electricity from renewables that is used to compress the working fluid of the HTHP cycle. After being

desuperheated, condensed and subcooled in the cascaded SH-PCM thermal energy storage, the working fluid is throttled to the evaporation pressure by means of an isenthalpic Joule-Thomson process and then evaporated in a dedicate heat exchanger using either an environmental heat source or any available waste heat sources. During discharge HTHP is switched off and the ORC unit is activated. The liquid working fluid of the ORC unit is forwarded by the pump to the heat addition process, where it is preheated, vaporized and superheated by transferring heat with the SH-PCM thermal energy storage. The working fluid is then expanded in a turbine and condensed back by exchanging heat at low temperature with the environment.

Applying the same concept of combining different materials for the TES to enhance the heat transfer process between the working fluid and TES but with a new technical strategy, a novel CHEST architecture is proposed (Fig. 3), representing an alternative to the baseline scenario proposed in literature. In particular, the cascaded SH-PCM thermal energy storage has been replaced by a compact cascaded PCM based thermal energy storage. The novel solution has the potential of considerably increasing the energy storage density of the TES, thus reducing space requirement and costs of the overall CHEST.

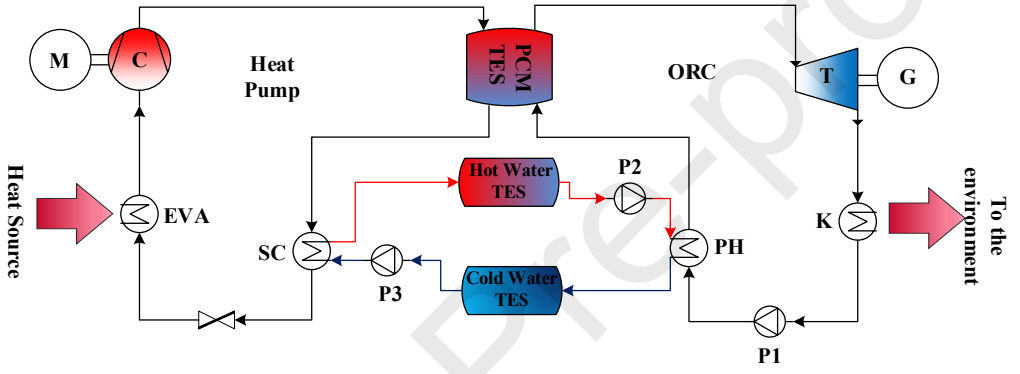

Fig. 2. CHEST process schematic – Baseline scenario (Adapted from [11]).

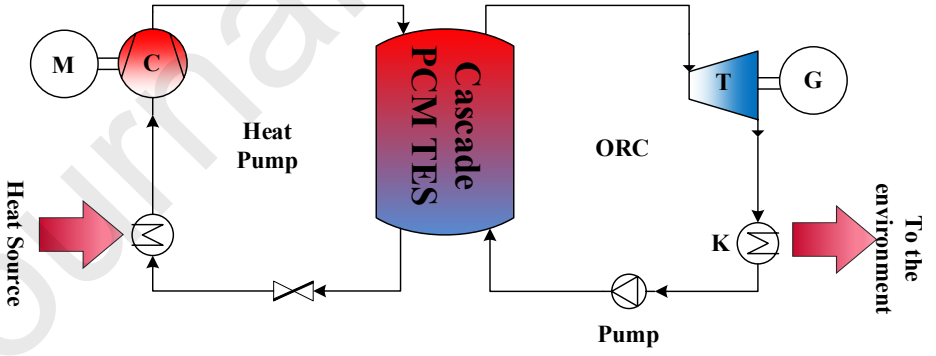

Fig. 3. CHEST process schematic – Novel case scenario.

3. Mathematical modelling

3.1. Thermal energy storage system model

The heat transfer process on the working fluid side of the charge and discharge phases can be broken down into a sensible heat part in the ORC preheater and the HTHP subcooler and a latent heat part in the

ORC evaporator and the HTHP condenser. To match the temperature profiles of the working fluid and heat transfer fluid (HTF) exchanging heat with the TES systems, two TES configurations have been adopted:

1) A combined pressurized water storage for the sensible part and a PCM storage for the evaporation and condensation (SH-PCM), representing the baseline case study, currently implemented in literature as shown in Section 1. Two pressurized water tanks were chosen for the sensible heat TES section; KNO_3-$LiNO_3$ was chosen as the filler medium for the phase change material (PCM1) section of the TES.
2) A cascade of three PCMs (3-PCM), the novel solution for the TES. Each PCM occupies one third of the TES and all are assigned the same latent heat and thermophysical properties as the PCM utilized in SH-PCM case. Nevertheless, different melting temperature were assumed for the 3 PCMs as shown in Table 1.

Table 1. Storage material properties.

Parameter		PCM-1	PCM-2	PCM-3	Unit
ρ_d, Density	Solid	1900	1900	1900	*kg/m³*
	Liquid	1900	1900	1900	
Specific heat	Solid	1.5	1.5	1.5	*kJ/kg K*
	Liquid	1.5	1.5	1.5	
Thermal conductivity	Solid	0.5	0.5	0.5	*W/m K*
	Liquid	0.5	0.5	0.5	
Latent heat		167.3	167.3	167.3	*kJ/kg*
T_{m1}		132	119	107	*°C*
T_{m2}		134	121	109	*°C*
Particle diameter		0.015	0.015	0.015	*m*

In order to compare the different TES systems, the following assumptions were made:

- The aspect ratio of the TES tank and the operating conditions are the same for both studies and are based on the ORC design parameters (Table 2).
- Similarly, to the packed beds employed in concentrated solar plants, a cut-off criterion for the discharge phase ($T_{cut\text{-}off}$) was applied. Indeed, to ensure that the ORC unit is only operating above its minimum load (i.e. 20 % of the nominal value), a minimum threshold temperature of the HTF at the TES outlet is set: once this temperature limit was reached, the TES discharge process is considered terminated.
- The numerical results have been reported for steady state temperature profiles established in the TES, approximately after about 9 complete charging and discharging cycles.

Table 2. Technical input data for the TES system under study.

Parameters	Value	Unit
Aspect Ratio (H/D)	1.5	-
HTF, Heat Transfer Fluid	Therminol D-12	-
t_{ch}, charging time	9	*h*
t_d, discharging time	3	*h*

A detailed modeling approach for both the sensible heat and the PCM sections will be discussed in the following.

3.1.1. Sensible heat thermal energy storage

The sensible heat TES system is modeled by means of two pressurized water tanks at two different temperature levels. The pressurized water acts as a secondary HTF in the HTHP subcooler and in the ORC preheater. During the charge process, the water in the low temperature tank is heated up by the HTHP working fluid undergoing the subcooling process and delivered to the high temperature tank. The thermal power $\dot{Q}_{ch,SHTES}$ transferred during the charge process can be calculated as:

$$\dot{Q}_{ch,SHTES} = \dot{m}_{wat,ch} \cdot \Delta h_{wat,ch} = \dot{m}_{wat,ch} \cdot c_{p,wat,ch} \cdot \Delta T_{wat,ch} \quad (1)$$

where $\dot{m}_{wat,ch}$ is the water mass flow rate; $\Delta h_{wat,ch}$ is the enthalpy difference of the water due to the temperature difference $\Delta T_{wat,ch}$ and $c_{p,wat,ch}$ is the specific heat at constant pressure of the water.

Once the cycle is reversed and the discharge process starts, the hot water is pumped to the ORC preheater, cooled down by the ORC working fluid and stored in the low temperature tank. The thermal power rejected by the hot water to the ORC can be calculated as:

$$\dot{Q}_{d,SHTES} = \dot{m}_{wat,d} \cdot \Delta h_{wat,d} = \dot{m}_{wat,d} \cdot c_{p,wat,d} \cdot \Delta T_{wat,d} \quad (2)$$

Since the heat losses in the SH TES are neglected, the water temperature stored in the tanks is equal to the outlet temperature of the water pumped to the HTHP and the ORC units during the charge and discharge processes, respectively.

3.1.2. Phase change material thermal energy storage

A PCM TES packed bed configuration was chosen for its high surface/volume ratio. This leads to an enhancement of the heat transfer rate, particularly crucial for PCM characterized by low thermal conductivity [22]. In order to mathematically model the TES system, a concentric dispersion model was implemented to derive the thermal behaviour of the TES by using a MATLAB design routine previously presented and validated in Ref. [23] using the experimental results obtained from a test rig built for the purpose at TESLAB@NTU. The comparison between the numerical predictions of the charge and discharge HTF temperatures and the experimental results shows a good qualitative and quantitative agreement with an overall mean average percentage error less than 6 %. Additional and more exhaustive information can be found in Ref. [23].

The main assumptions of the numerical model are as follows:

- Isotropic PCM particles.
- Uniform distribution of porosity is applied within the TES packed bed.
- Internal heat generation and radiation are not considered within the TES packed bed.
- The HTF thermophysical properties are considered constant and calculated at an average temperature, $T_{ave} = \frac{T_{in} + T_{out}}{2}$.

Based on those assumptions, three unsteady one-dimensional energy equations were developed to calculate the transient temperature distribution of the HTF and the storage media within the thermal energy storage. More details of the mathematical model formulation can be found in [23].

For the HTF phase:

$$\varepsilon\rho_f c_{p,f}\left(\frac{\partial T_f}{\partial t}+u_f\frac{\partial T_f}{\partial x}\right)=\varepsilon k_f\frac{\partial^2 T_f}{\partial x^2}+h_{fp}a_s(T_s-T_f)+\frac{U_w D\pi}{A_{bed}}(T_{amb}-T_f) \quad (3)$$

where ε is the porosity of the packed bed; k_f, c_{pf} and ρ_f are the thermal conductivity, heat capacity and density of the HTF, respectively; u_f is the interstitial velocity of the HTF; T_s and T_f are the temperatures of the storage medium phase and the HTF, respectively; h_{fp} is the volumetric heat transfer coefficient between the storage medium phase and the HTF; U_w is the overall heat transfer coefficient of the heat losses to the environment; A_{bed} and D are the frontal area and the diameter of the packed bed, respectively.

For the solid phase:

$$(1-\varepsilon)\rho_s c_{p,p}\frac{\partial T_s}{\partial t}=(1-\varepsilon)k_p\frac{\partial^2 T_s}{\partial x^2}+h_{fp}a_s(T_f-T_s) \quad (4)$$

For the PCM particles:

$$\rho_p c_{p,p}\frac{\partial T_p}{\partial t}=k_p\left(\frac{\partial^2 T_p}{\partial r^2}+\frac{2\partial T_p}{r\,\partial r}\right) \quad (5)$$

where k_p, $c_{p,p}$ and ρ_p are the thermal conductivity, heat capacity and density of the particles, respectively

The thermodynamic properties of the PCM particles were defined among three phases, namely solid, solid-liquid transition, and liquid phases:

$$c_{p,p}=\begin{cases}c_{p,s} & T_p > T_{m2}\\ \frac{(c_{p,s}+c_{p,l})}{2}+\frac{L}{T_{m2}-T_{m1}} & T_{m1}<T_p\le T_{m2}\\ c_{p,l} & T_p\le T_{m1}\end{cases} \quad (6)$$

$$k_p=\begin{cases}k_s & T_p > T_{m2}\\ \frac{(k_s+k_l)}{2} & T_{m1}<T_p\le T_{m2}\\ k_l & T_p\le T_{m1}\end{cases} \quad (7)$$

The heat transfer coefficient between the heat transfer fluid and the particles (h_{fp}) is calculated using the correlation developed by Wakao et al. [24]:

$$Nu=\frac{h_{fp}d_p}{k_f}=2+1.1Pr^{\frac{1}{3}}Re_p^{0.6} \quad (8)$$

where d_p is the particle diameter and Pr and Re_p are the Prandtl number and the Reynolds number, respectively, defined as:

$$Pr=\frac{c_{pf}\mu_f}{k_f};\ Re_p=\frac{\rho_f d_p\varepsilon u_f}{k_f} \quad (9)$$

In order to further enhance intra-particle diffusion during PCM solidification and melting, according to Zanganeh et al. [25], an effective heat transfer coefficient has been introduced replacing the fluid-particle heat transfer coefficient h_{fp} :

$$h_{fp,eff} = \frac{h_{fp}}{1 + 0.25Bi} \tag{10}$$

where Bi is the Biot number defined as:

$$Bi = \frac{h_{fp} d_p}{6k_p} \tag{11}$$

The correlation proposed by Mertens et al. [26] was adopted to estimate the porosity of the bed (ε):

$$\varepsilon = 1 - \frac{V_p}{V_{tot}} = 0.375 + 0.17\frac{d_p}{D} + 0.39\left(\frac{d_p}{D}\right)^2 \tag{12}$$

To solve the mathematical problem represented by Eqs. (3-5), boundary conditions and initial conditions need to be specified:

$$T_f(x=0) = T_{in};\ \frac{\partial T_f}{\partial x}(x=H) = 0;\ T_p(x=0) = T_{in};\ \frac{\partial T_p}{\partial x}(x=H) = 0 \tag{13}$$

$$T_f(t=0) = T_{in};\ T_s(t=0) = T_o \tag{14}$$

$$\left.\frac{\partial T_p}{\partial r}\right|_{r=0} = 0; T_p\left(r=\frac{R}{2}\right) = T_s \tag{15}$$

The governing partial differential equations (PDEs) along with the boundary and initial conditions were solved by MATLAB software using finite difference method (FDM) under the fully implicit scheme. The first order upwind scheme is used to discretize the temporal and advective term, while second-order central differencing is used to discretize the diffusion term in Eqs. (3-5). The discretization of the computational domain was performed with a uniform grid along the flow direction.

3.2. ORC model

The ORC unit was designed by using a MATLAB design routine previously presented and validated in Refs. [27,28]. A comparison with a Dymola model showed deviations below 2 % in net power [27] . A validation with an existing ORC unit provided a maximum deviation in net power output of 10 % in the operating range from 40 % to 100 % of the nominal load [28].

In this work, the design and off-design routines have not been integrated in the same global optimization loop but used sequentially for simplicity. A subcritical ORC unit without recuperator is considered here. The design routine is based on steady-state mass and energy balances on control volumes around the main ORC components:

$$\dot{m}_{wf,in} = \dot{m}_{wf,out} = \dot{m}_{wf} \tag{16}$$

$$\dot{m}_{wf,in} h_{wf,in} + \dot{Q} - \dot{W} = \dot{m}_{wf,out} h_{wf,out} \tag{17}$$

where $\dot{m}_{wf}$ is the mass flow rate and h_{wf} is the specific enthalpy of the working fluid. $\dot{Q}$ is the heat transfer rate from the heat source ($\dot{Q} > 0$) or heat sink ($\dot{Q} < 0$) into the control volume and $\dot{W}$ the mechanical power transferred to the turbine ($\dot{W} > 0$) or pump ($\dot{W} < 0$). The subscripts 'in' and 'out' refer to the incoming and outgoing working fluid streams with respect to the control volume.

The thermal energy stored in the PCM is transferred to the ORC unit by means of a thermal oil (Therminol D-12), whereas the thermal energy in the sensible heat thermal energy storage is stored in pressurized water at 10 bar. In other words, two heat sources are available for the ORC unit in the baseline cascade SH-PCM case (i.e. thermal oil from PCM and pressurized water from the sensible heat TES), whereas the thermal oil from the PCM is the only heat source in the novel 3-PCM case. The heat sink for the ORC unit is water at 20 °C and 1 bar.

Pressure and heat losses in the ORC system were neglected in the numerical model. The heat exchangers were discretized in control volumes according to the number of phases (liquid, two-phase and vapour). Given the design temperatures of the heat sources and heat sink, together with the fixed net power output of 1 MW_e, the net electrical efficiency of the ORC unit was maximized by finding the optimal set of decision variables, e.g., the evaporation pressure, specific enthalpy at turbine inlet, pinch-point temperature difference at the evaporator and condenser, condensation temperature and mass flow rate of the heat sources. The specific enthalpy at turbine inlet is normalized according to:

$$h^*_{wf,T,in} = \frac{h_{wf,T,in} - h'_{wf}}{h''_{wf} - h'_{wf}} \tag{18}$$

where h''_{wf} and h'_{wf} are the specific enthalpy at saturated vapour and liquid respectively. The subscript 'T' refers to the turbine. The normalized specific enthalpy is chosen because it allows for a simple extension of future analyses to partial evaporation cycles ($h^*_{wf,T,in} < 1$), although in this work $h^*_{wf,T,in} \geq 1$. The net power output of the ORC unit is fixed to 1 MW_e and calculated as follows:

$$\dot{W}_{net,ORC} = \dot{W}_T \eta_G + \frac{\dot{W}_P}{\eta_{PM}\eta_{PI}} = \dot{m}_{wf} \left(h_{wf,T,in} - h_{wf,T,out}\right) \eta_G - \dot{m}_{wf} \frac{h_{wf,P,in} - h_{wf,P,out}}{\eta_{PM}\eta_{PI}} \tag{19}$$

where η_G, η_{PM} and η_{PI} are the efficiencies of the electric generator and pump ('P') electric motor, pump frequency converter, which were set to the exemplary values of respectively 90 %, 85 % and 95 %. To estimate the isentropic efficiency of the turbine, the correlations of Macchi and Astolfi [29] for single-stage turbines were used. The isentropic efficiency of the pump at design was fixed to 70 % [30].

The objective function to maximize is the net electrical efficiency $\eta_{el,net}$, defined as follows:

$$\eta_{el,net,ORC} = \frac{\dot{W}_{net,ORC}}{\dot{Q}_{d,TES}} \tag{20}$$

where $\dot{Q}_{d,TES}$ is the overall heat transfer rate from the thermal energy storage to the ORC unit.

Table 3 summarized the ORC decision variables and reports the upper and lower bounds set in the design optimization routine. The derivative-free optimization function 'patternsearch' from the MATLAB Optimization Toolbox was used, with a step and function tolerance of 1e-6 and a constraint tolerance (necessary to find the required net power output) fixed to 1e-4. The input parameters, constraints and objective function are summarized in Table 4.

Table 3. Decision variables for ORC design routine.

Decision variables	Lower bound	Upper bound	Unit
Evaporation pressure	4.0	32.1	*bar*
Normalized specific enthalpy at turbine inlet	1.0	1.5	-
Pinch-point temperature difference at evaporator	5.0	20.0	*K*
Pinch-point temperature difference at condenser	5.0	20.0	*K*
Condensation temperature	25.0	40.0	*°C*
Mass flow rate of heat source (thermal oil)	50.0	80.0	*kg/s*
Mass flow rate of heat source (hot water)*	0.1	50.0	*kg/s*

*Only for the SH-PCM TES.

Table 4. Input parameters, constraints and objective function for ORC design routine.

Parameters	Value	Unit
Inlet temperature of thermal oil	140.0	*°C*
Inlet temperature of hot water*	133.0	*°C*
Outlet temperature of hot water*	45.0	*°C*
Number of turbine expansion stages	1.0	-
Electric generator efficiency	90.0	*%*
Pump isentropic efficiency	70.0	*%*
Pump motor efficiency	85.0	*%*
Pump inverter efficiency	95.0	*%*
Inlet temperature of cold water	20.0	*°C*
Constraints		
No temperature crossings among working fluid and heat sources / sink		
Minimum change of temperature for the cold water equal to 3 K		
Net power output equal to 1 MW_e		
Objective function		
Maximum net electrical efficiency (Eq. 20)		

*Only for the SH-PCM TES.

After a preliminary screening of possible working fluids, Isobutene was identified as suitable candidate, given its low environmental impact, high thermal stability and good thermodynamic performance. It has an almost isentropic vapor saturation line and a suitable critical temperature (145 °C) for the available PCMs. The fluid properties were retrieved using REFPROP 10.0 [31].

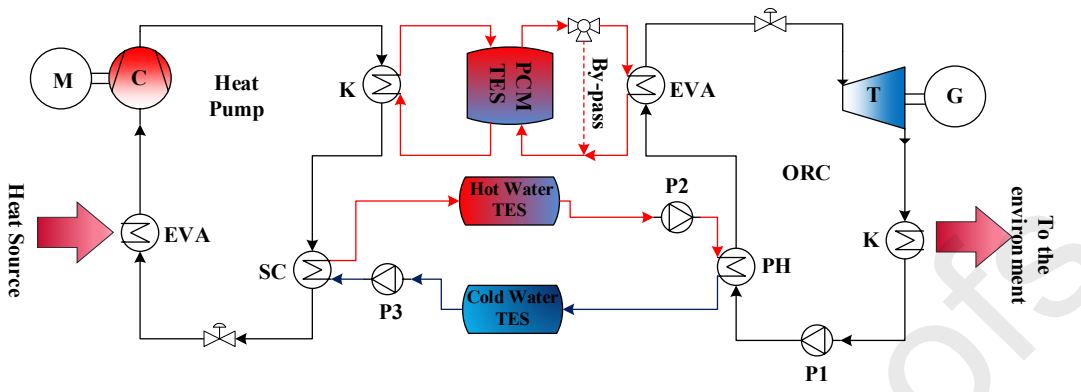

Fig. 4. CHEST P&ID diagram for partial load control – Baseline case scenario.

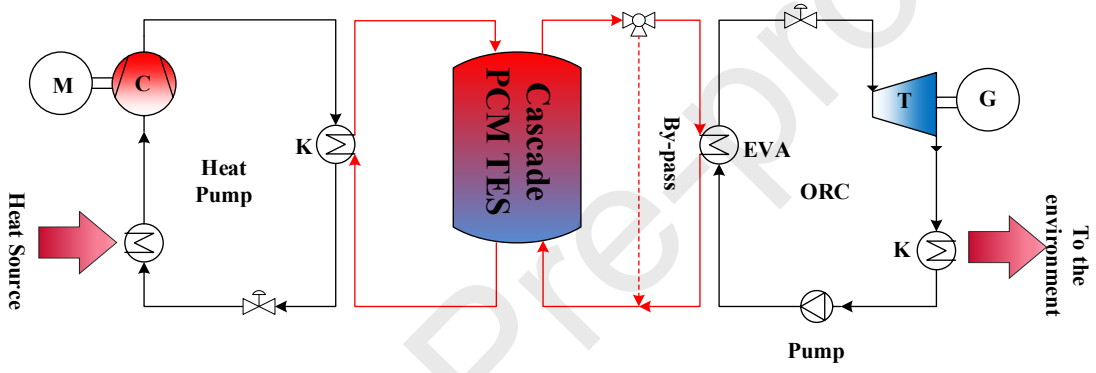

Fig. 5. CHEST P&ID diagram for partial load control – Novel case scenario.

The state of charge of the PCM-TES defines the temperature of the thermal oil leaving the PCM and entering the ORC evaporator. In particular, as the discharge process proceeds, the temperature of the thermal oil reaching the ORC unit decreases over time. The deviation of the oil inlet temperature from the design point causes the ORC unit also to work away from the design point. In order to maximize the ORC net power output at any operating point, the part-load optimization routine in Ref. [27] was used. In particular, as shown in Fig. 4 and Fig. 5, the net power output of the ORC (Eq. 19) was maximized by acting: 1) on the mass flow rate of the working fluid; 2) on the mass flow rate of the cooling medium at the ORC condenser; 3) on the opening of a control valve at turbine inlet; 4) on the opening of bypass valve of the thermal oil at the inlet of the ORC unit and 5) on the mass flow rate of the hot water for the sensible heat TES. As a result, the optimal operating conditions (evaporation and condensation pressure, degree of superheating, etc.) ensuring the maximum net power output were achieved. A summary of the decision variables for the part-load optimization and their upper and lower bounds is reported in Table 5. To allow for a simple control of the heat transfer rate from the TES to the ORC unit, the mass flow rate and the return temperature of the thermal oil to the TES are fixed at the design value. The part-load optimization routine is based on the optimization function ‘fmincon’ available from the MATLAB Optimization Toolbox. Among the available algorithms for the ‘fmincon’ function, the SQP algorithm was chosen, because it was found to converge better to the optimal solution for the current optimization problem. A detailed description of the SQP algorithm and the other MATLAB algorithms is out of the scope of the present work and can be found in Ref [32]. The step, function and constraint tolerances for the current optimization problem were set to 1e-4. The input parameters, constraints and objective function for the part-load optimization are summarized in Table 9.

Table 5. Decision variables for ORC part-load optimization.

Parameters	Lower bound	Upper bound	Unit
Mass flow rate of working fluid	20 % of design	100 % of design	*kg/s*
Mass flow rate of cooling medium	20 % of design	120 % of design	*kg/s*
Opening of throttle valve at turbine inlet	0.0	100.0	*%*
Fraction of mass flow rate of heat source bypassed (thermal oil)	0.0	100.0	*%*
Fraction of mass flow rate of heat source bypassed (hot water)*	0.0	100.0	*%*

*Only for the SH-PCM storage.

Table 6. Input parameters and constraints for ORC part-load optimization.

Parameters
Heat transfer area of condenser
Heat transfer area of preheater*
Heat transfer area of evaporator
Part-load exponents for heat exchangers
Turbine part-load characteristics
Inlet temperature of cold water at 20 ºC
Constraints
No temperature crossings among working fluid and heat sources / sink
Full evaporation and condensation of working fluid
Outlet temperature and mass flow rate of heat source from TES equal to design value
Objective function
Maximum net power output (Eq. 19)

*Only for the SH-PCM TES.

The part-load optimization routine requires knowledge about the heat transfer area and heat transfer coefficients of the heat exchangers. Also here, the heat exchangers are discretized in control volumes based on the phase of the working fluid (liquid, two-phase and vapour). The area of each control volume at part-load can vary, but the total area of the heat exchanger is fixed. Analogously to what was done in Ref. [27], Aspen Exchanger and Design Rating [33] was used to evaluate the heat transfer coefficients, using the results of the ORC design routine as input to the heat exchanger design. At part-load, the overall heat transfer coefficients U are corrected compared with the design value by the exponential law:

$$U_{OD} = U_D \sum_{i=1}^{N} \left(\frac{x_{i,OD}}{x_{i,D}} \right)^{\tau_i} \tag{21}$$

where x_i is a correction parameter, N is the total number of parameters (typically $N = 1$ for simplicity) and τ_i an exponent fitted from simulation data. The subscripts 'D' and 'OD' refer to design and off-design operating conditions.

The part-load efficiency of the turbine is corrected from the design value according to the part-load correlations for single-stage axial-flow turbines developed in Ref [34]. The part-load efficiency of the electric generator, the pump, the pump motor and the inverter are reported in Ref. [27].

3.3. Heat Pump model

The HTHP model is also written in MATLAB and is highly based on the ORC model. The model uses the same steady-state mass and energy balances on control volumes around the main components according to the working fluid phase (Eqs. 16-18). The turbine and the pump used in the ORC model are replaced by the isenthalpic expansion valve and the compressor of the heat pump. Based on literature [35], the isentropic efficiency of the compressor at design conditions is set to 80 %, while its motor and frequency converter have efficiencies of 90 % and 95 %. Note that the motor efficiency for the compressor is higher than the motor efficiency for the ORC pump (90 % vs 85 %) because of its larger size (MW_e vs hundreds of kW_e). The heat source of the heat pump is waste heat in the form of hot water at 85 °C and 10 bar, with a specified minimum temperature change of 5 K. The heat sink consists of the TES and depends on the case under study (SH-PCM or cascaded PCM). In the baseline case SH-PCM, heat is provided by the HTHP to both the thermal oil for the PCM and the hot water for the sensible heat storage. In the novel cascaded PCM, the thermal oil is the only heat sink of the heat pump. Given its good thermodynamic and environmental properties, the same working fluid is selected as for the ORC unit (isobutene).

The decision variables for the HTHP design are analogous to the ones used for the ORC unit: the evaporation temperature, specific enthalpy at condenser outlet and evaporator outlet, pinch-point temperature difference at the evaporator and condenser and condensation temperature. The mass flow rate of the heat sources is now constrained by the required thermal energy that the heat pump needs to supply to the TES systems and is already known before the design routine starts. Analogously to the ORC design, the specific enthalpies at condenser and evaporator outlets are normalized following Eq. (18). Table 7 summarizes the decision variables and reports the upper and lower bounds used in the design optimization routine of the HTHP, while Table 8 reports the input parameters, constraints and objective function used. Similarly, to the ORC design routine, the derivative-free optimization function ‘patternsearch’ from the MATLAB Optimization Toolbox was used, with a step and function tolerance of 1e-6 and a constraint tolerance (necessary to find the required heat transfer rate to the TES) equal to 1e-4.

Table 7. Decision variables for HTHP design routine.

Parameters	**Lower bound**	**Upper bound**	**Unit**
Evaporation temperature	10.0	80.0	*°C*
Normalized specific enthalpy at condenser outlet	-2.0	0.0	-
Normalized specific enthalpy at evaporator outlet	1.0	1.2	-
Pinch-point temperature difference at evaporator	5.0	20.0	*K*
Pinch-point temperature difference at condenser	5.0	20.0	*K*
Condensation temperature	100.0	300.0	*°C*

Table 8. Input parameters and constraints for HTHP design routine.

Parameters	**Value**	**Unit**
Inlet temperature of thermal oil	116.9* / 95.6**	*°C*
Outlet temperature of thermal oil	140.0	*°C*
Mass flow rate of thermal oil	24.4* / 23.6**	*kg/s*
Inlet temperature of hot water*	45.0	*°C*
Outlet temperature of hot water*	133.0	*°C*
Mass flow rate of hot water*	2.85	*kg/s*
Compressor isentropic efficiency	80.0	*%*
Compressor motor efficiency	90.0	*%*
Compressor inverter efficiency	95.0	*%*
Inlet temperature of heat source	85.0	*°C*
Constraints		
No temperature crossings among working fluid and heat sources / sink		
Minimum change of temperature for the heat source equal to 5 K		
Objective function		
Maximum coefficient of performance (COP, Eq. 22)		

*Only for the SH-PCM TES.

** Only for cascaded PCM TES.

The objective of the design routine is to maximize the Coefficient of Performance (COP) of the HTHP, defined by:

$$COP = \frac{\dot{Q}_{ch,TES}}{-\dot{W}_{HTHP}} = \frac{\dot{Q}_{ch,TES}}{-\dot{W}_C/(\eta_{CM}\eta_{CI})} = \frac{\dot{Q}_{ch,TES}}{\dot{m}_{wf}(h_{wf,C,out} - h_{wf,C,in})/(\eta_{CM}\eta_{CI})} \tag{22}$$

where $\dot{Q}_{ch,TES} > 0$ is the heat transfer rate to the TES, $\dot{W}_C < 0$ is the mechanical power transferred between the compressor's moving parts and the working fluid, and η_{CM} and η_{CI} refer to the efficiencies of the compressor electric motor and inverter.

The part-load operation of the HTHP is defined by the thermal oil inlet temperature to the heat pump, whereas the mass flow rate of the thermal oil is fixed at design value, for simplicity. In the baseline SH-PCM case, the mass flow rate of the sensible storage water is adjusted in order to keep the same thermal energy ratio between the PCM and the sensible heat as during the ORC discharge. This ensures that both the PCM and SH storage are fully charged at the end of the charging process.

The part-load model of the HTHP is analogous to the ORC part-load model. As in the design routine, the heat exchangers are discretized in control volumes according to the working fluid phase. The heat transfer area and the heat transfer coefficients are retrieved from Aspen Exchanger Design and Rating. The heat transfer coefficients are corrected to account for part-load operation following Eq. (21). The power law exponent is fitted from the simulation results with Aspen Exchanger Design and Rating at part-load. The isentropic efficiency of the compressor at part-load follows Eq. (23) [36]:

$$\eta_{is,C,OD} = \eta_{is,C,D}\left[\pi_{OD}^{(\kappa-1)/\kappa} - 1\right] / \left[\pi_D^{\frac{\kappa-1}{\kappa}} - \frac{\kappa-1}{\kappa}\pi_D^{-\frac{1}{\kappa}}(\pi_D - \pi_{OD}) - 1\right] \tag{23}$$

where κ is the ratio of the specific heats at compressor inlet, $\pi = p_{wf,cond}/p_{wf,eva}$ is the pressure ratio of the compressor, and $\eta_{is,C,D}$ is the design isentropic efficiency of the compressor. The part-load efficiencies of the compressor electric motor and inverter efficiencies are corrected with the same equations of the pump electric motor and inverter.

The decision variables for the part-load COP optimization of the HTHP are: 1) the mass flow rate of the working fluid; 2) the mass flow rate of the heat source at the HTHP evaporator; 3) the difference between the evaporation pressure and 4) the condensation pressure. As a result, the optimal operating conditions (evaporation and condensation temperatures, degree of superheating, subcooling, etc.) ensuring the maximum COP were achieved. The decision variables for the part-load optimization of the HTHP and their upper and lower bounds are reported in Table 9, while the input parameters, constraints and objective function are summarized in Table 10. The optimal opening of the expansion valve, although not determined here because not relevant for the present analysis, can be defined by matching the valve part-load characteristics with the difference between the optimal evaporation and condensation pressures together with the optimal mass flow rate of the working fluid. Analogously to the ORC case, the part-load optimization routine is based on the optimization function 'fmincon' available from the MATLAB Optimization Toolbox, using the SQP algorithm. The step, function and constraint tolerances were set to 1e-4.

Table 9. Decision variables for HTHP part-load optimization.

Parameters	**Lower bound**	**Upper bound**	**Unit**
Mass flow rate of working fluid	20 % of design	100 % of design	*kg/s*
Mass flow rate of heat source medium	20 % of design	100 % of design	*kg/s*
Evaporation pressure	6.1	36.5	*bar*
Condensation pressure	6.1	36.5	*bar*

Table 10. Input parameters and constraints for HTHP part-load optimization.

Parameters
Heat transfer area of condenser
Heat transfer area of desuperheater*
Heat transfer area of evaporator
Part-load exponents for heat exchangers
Compressor part-load characteristics
Inlet temperature of heat source at 85 ºC
Constraints
No temperature crossings among working fluid and heat sources / sink
Full evaporation and condensation of working fluid
Outlet temperature of and mass flow rate of thermal oil equal to design value
Heat rate ratio between heat sources set as for ORC*
Objective function
Maximum coefficient of performance (COP, Eq, 22)

*Only for the SH-PCM TES.

3.4. Key performance indicators

The results of the simulations will be presented in the next section with reference to the following performance parameters.

In order to compute the performance of the HTHP during the entire charge phase, the average COP is introduced as:

$$COP_{HTHP} = \frac{\int_0^{t_{ch}} \dot{Q}_{ch,\mathrm{TES}}\, dt}{\int_0^{t_{ch}} \dot{W}_{HTHP}\, dt} \tag{24}$$

The ORC thermodynamic efficiency evaluates the performance of the discharge phase:

$$\eta_{\mathrm{ORC}} = \frac{\int_0^{t_{\mathrm{d}}} \dot{W}_{net,\mathrm{ORC}}\, dt}{\int_0^{t_{\mathrm{d}}} \dot{Q}_{\mathrm{d,TES}}\, dt} \tag{25}$$

The premier key performance indicator of the CHEST energy storage system is represented by the round trip efficiency, computed as follows:

$$\eta_{\mathrm{RT}} = \frac{\int_0^{t_{\mathrm{d}}} \dot{W}_{net,\mathrm{ORC}}\, dt}{\int_0^{t_{ch}} \dot{W}_{HTHP}\, dt} \tag{26}$$

Energy density φ [kWh_e/m^3] is calculated as the ratio between the electrical energy produced and the volume of the TES:

$$\varphi = \frac{E_{el,ORC}}{V_{TES}} \tag{27}$$

4. Results and discussion

4.1. Design and part-load performance of the CHEST system

The overall design and performance evaluation procedure of the CHEST system is illustrated in Fig. 6. The general structure of the algorithm is analogous for the SH-PCM and the 3-PCM cases. The algorithm

At first, the ORC unit was designed by using the numerical model and the specifications defined in Section 3.2. In this way, the mass flow rates of the heat sources to achieve 1 MW_e of net power output with maximum net electric efficiency were determined.

The mass flow rates of the thermal oil and the hot water (the latter only for the SH-PCM) case coming from the ORC design routine were used together with the assumptions and the numerical models provided in Section 3.1.1 and Section 3.1.2 to design the SH-PCM and the 3-PCM TES systems. In particular, the volume and the mass of the storage material were defined. After the design, the dynamic model of the TES was used to define the change of the temperature of thermal oil leaving the storage over time. The return temperature of the thermal oil drops during discharging whereas it gradually increases during charging.

By knowing the range of variation of the return temperature of the thermal oil from the TES to the ORC unit during discharging, it was possible to optimize the part-load operation of the ORC unit. To achieve this goal, the range of possible return temperatures of the thermal oil was discretized in a uniform grid of n = 16 values. The net power output of the ORC unit was optimized for each of the part-load operation points, thus achieving an optimal part-load performance map of the ORC unit. The performance between the part-load grid points was assessed by means of linear interpolation.

At this point, by knowing the TES performance and requirements it was possible to design the HTHP unit crucial for the charging process. The HTHP design routine used the numerical model, assumptions and

constraints provided in Section 3.3. Once the design was completed, the part-load operation of the HTHP unit was optimized for maximum COP. The part-load operation was optimized on a uniform grid of n = 16 operating points that cover the range of variation of the return temperature of the thermal oil during charging. This range was provided by the dynamic simulation of the TES charging process. The HTHP COP was maximized for each of the part-load operating points. In order to balance the sensible energy stored during charging with the one released during discharging, the mass flow rate of the hot water was adjusted in the SH-PCM case by keeping the ratio between the heat transfer rate between the working fluid and the hot water and the heat transfer rate between the working fluid and the thermal oil equal to the ratio that was defined for the ORC unit during discharging.

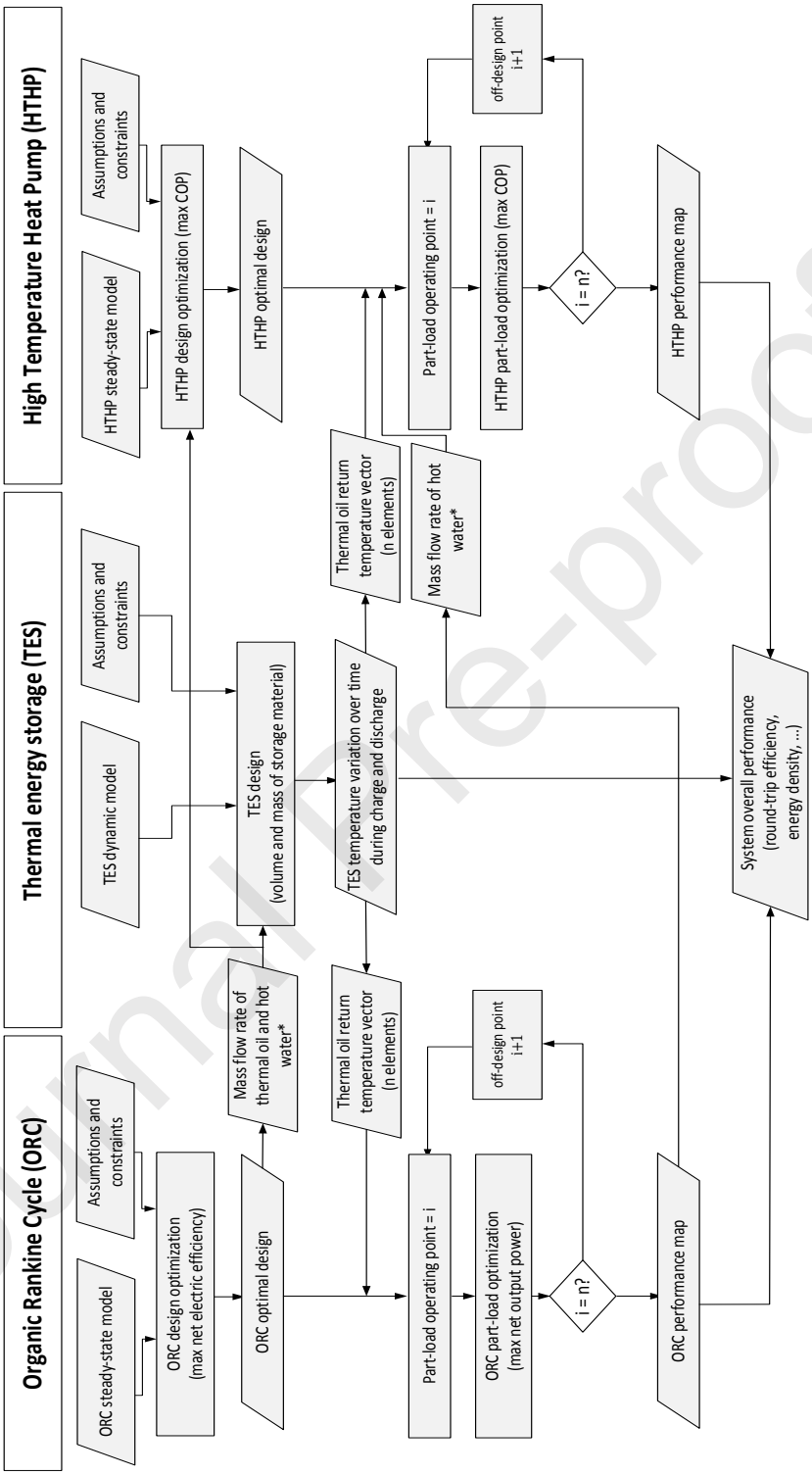

Fig. 6. CHEST design and part-load optimization algorithm.

4.1.1. ORC unit

The ORC unit was designed by using the MATLAB design routine described in section 3.2 for both the SH-PCM and 3-PCM cases. The most important results of the design optimization are collected in Table 11. It can be seen that the design conditions for the SH-PCM and 3-PCM are very similar. This is confirmed by the T-s diagrams in Fig. 7. Both solutions require the pinch-point temperature differences at the evaporator and condenser to be at the lower bound of 5 K in order to maximize the net electrical efficiency. The pinch-point actually occurs simultaneously at two points of the evaporator: at the saturated liquid point and at the outlet of the working fluid. This results in a maximum temperature of the working fluid for both case studies equal to 135 °C. The pinch-point at the condenser occurs instead at the saturated vapour state. The condensation temperature is also close to the lower bound of 25 °C but slightly higher (27.5 °C) because of the temperature increase of the cooling medium when flowing from the inlet towards the outlet of the condenser (note that a minimum temperature increase of 3 K was imposed to the cooling medium in order to set an upper limit to the mass flow rate). In terms of decision variables, the two solutions only differ in evaporation pressure (3 % lower in the 3-PCM case). The lower evaporation pressure of the 3-PCM case requires a larger mass flow rate of working fluid (by 0.6 %) to fulfill the constraint of fixed net power output equal to 1 MWe. Since the turbine is subjected to a slightly lower pressure ratio and larger volume flow rate in the 3-PCM case, which is beneficial for the turbine performance, its isentropic efficiency is slightly higher (0.1 % absolute). The differences are nonetheless very small. The net electrical efficiency for both ORC units is close to what reported by Ref. [37] at comparable heat source temperature of 140 ºC and considering a 90 % efficiency of the electric generator. Ref. [37] shows a 14.5 % gross efficiency which would lead to approximately 13 % of net electric efficiency compared with the 12.7 % and 12.8 % achieved in the present work for respectively the SH-PCM and 3-PCM cases.

Table 11. Optimum design variables for ORC unit.

Parameters	**SH-PCM**	**3-PCM**	**Unit**
Evaporation pressure	22.7	22.0	*bar*
Normalized specific enthalpy at turbine inlet	1.3	1.3	-
Pinch-point temperature difference at evaporator	5.0	5.0	*K*
Pinch-point temperature difference at condenser	5.0	5.0	*K*
Condensation temperature	27.5	27.5	*°C*
Mass flow rate of heat source (thermal oil)	73.32	70.85	*kg/s*
Mass flow rate of heat source (hot water)	9.36	-	*kg/s*
Mass flow rate of working fluid	15.4	15.5	*kg/s*
Isentropic efficiency of turbine	86.3	86.4	*%*
Net power output	1.0	1.0	MW_e
Net electrical efficiency	12.8	12.7	*%*

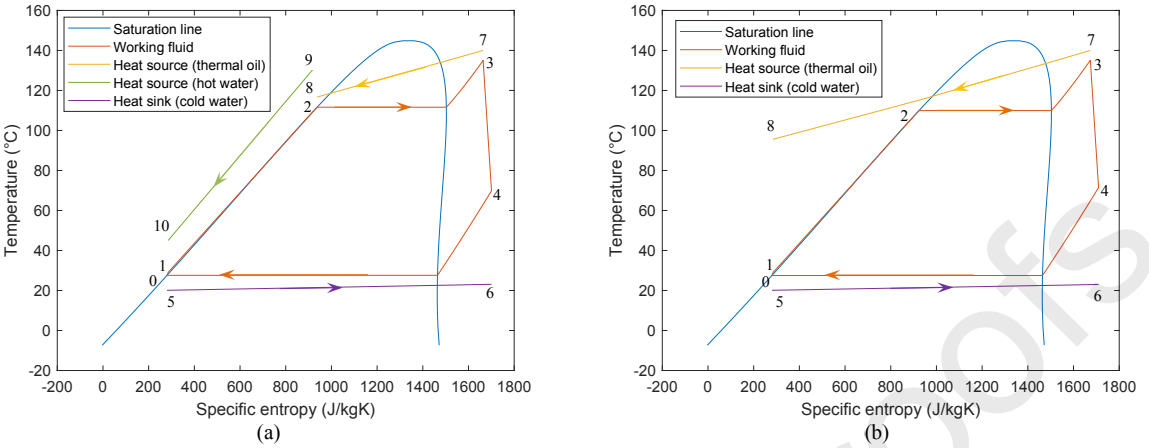

Fig. 7. T-s diagram of ORC design conditions – (a) baseline SH-PCM case and (b) 3-PCM case.

Using the results of the thermodynamic design routine, the heat exchangers of the ORC unit were designed and their part-load behaviour was approximated by means of exponential functions. The heat transfer coefficients and part-load exponents derived from the fitting (the procedure is described in Ref. [27]) are reported in Table 12 and Table 13. It can be seen that the two cases differ mainly in the presence of the hot water preheater for the SH-PCM case, whereas the heat transfer coefficients and exponents for the evaporator and the condenser are the same for both cases, thanks to the very similar operating conditions.

Table 12. Heat exchanger parameters of ORC unit (SH-PCM case).

Heat exchanger	**Phase**	**Heat transfer area,** m^2	**Overall heat transfer coefficient,** W/m^2K	**Part-load parameter**	**Part-load exponent, -**
Evaporator (thermal oil)	Liquid	0.0	121.8	$\dot{m}_{oil}$	0.29
	Two-phase	742.2	381.3	$\dot{m}_{oil}$	0.20
	Vapour	567.1	146.7	$\dot{m}_{wf}$	0.68
	Total	1309.3	-	-	-
Preheater (hot water)	Liquid	358.3	612.4	$\dot{m}_{hw}, \dot{m}_{wf}$	0.25, 0.34
	Two-phase	-	-	-	-
	Vapour	-	-	-	-
	Total	358.3	-	-	-
Condenser	Liquid	1.0	620.8	$\dot{m}_{wf}$	0.37
	Two-phase	992.5	900.3	$\dot{m}_{wf}$	0.15
	Vapour	164.1	383.0	$\dot{m}_{cw}$	0.48
	Total	1543.4	-	-	-

Table 13. Heat exchanger parameters of ORC unit (3-PCM case).

Heat exchanger	Phase	Heat transfer area, m^2	Overall heat transfer coefficient, W/m^2K	Part-load parameter	Part-load exponent, -
Evaporator (thermal oil)	Liquid	1187.5	121.8	$\dot{m}_{oil}$	0.29
	Two-phase	753.0	381.3	$\dot{m}_{oil}$	0.20
	Vapour	588.6	146.7	$\dot{m}_{wf}$	0.68
	Total	2529.0	-	-	-
Condenser	Liquid	0.1	620.8	$\dot{m}_{wf}$	0.37
	Two-phase	1002.2	900.3	$\dot{m}_{wf}$	0.15
	Vapour	167.3	383.0	$\dot{m}_{cw}$	0.48
	Total	1559.5	-	-	-

Based on the results of the thermodynamic and heat exchanger design procedures, the part-load of the ORC unit was optimized for a set of inlet temperatures of the thermal oil ranging from the design value of 140 °C down to the cut-off temperature, which differs between the SH-PCM and 3-PCM case studies. In fact, it can be seen in Fig. 8 that the part-load response between the SH-PCM and the 3-PCM case studies is quite different. The net power output $\dot{W}_{net,ORC}$ has a much sharper drop in the SH-PCM case as the inlet temperature of the thermal oil drops, leading to a necessary shut down of the ORC unit at 125 °C (the net power output would go below 20 % of the nominal value). The 3-PCM system, instead, can still produce 55 % of its installed capacity at 120 °C (0.55 MW_e). The net electrical efficiency $\eta_{el,net,ORC}$ follows the same trend, dropping from 12.8 % at 140 °C to 0.6 % at 125 °C in the SH-PCM case, whereas the drop is only from 12.7 % to 10.5 % in the cascaded PCM case. Furthermore, the total heat transfer rate $\dot{Q}_{d,TES}$ from the TES to the ORC unit also drops more significantly for the SH-PCM case compared with the 3-PCM case, from 7.9 MW_{th} at 140 °C to 3.2 MW_{th} at 125 °C. For the cascaded PCM case instead, the heat transfer rate with the thermal oil drops from 7.9 MW_{th} at 140 °C to 4.3 MW_{th} at 120 °C.

The reason for the different part-load performance between the SH-PCM and the 3-PCM case is due to the evaporator design and the constraint of fixed outlet temperature of the heat sources leaving the ORC unit. In the SH-PCM case, both the outlet temperature of the pressurized water and the outlet temperature of the thermal oil are fixed. As the inlet temperature of the thermal oil drops during the discharge process, it is necessary to reduce drastically the mass flow rate of working fluid, otherwise the temperature of the thermal oil leaving the ORC unit would also drop. In turn, the reduction of mass flow rate of working fluid requires the mass flow rate of the pressurized water also to be reduced, otherwise its outlet temperature would drop below the value set for the lower temperature tank. In other words, the condition of fixed outlet temperature of the hot water and thermal oil requires the mass flow rate of working fluid to drop significantly at part-load, resulting in a strong of reduction of $\dot{W}_{net,ORC}$.

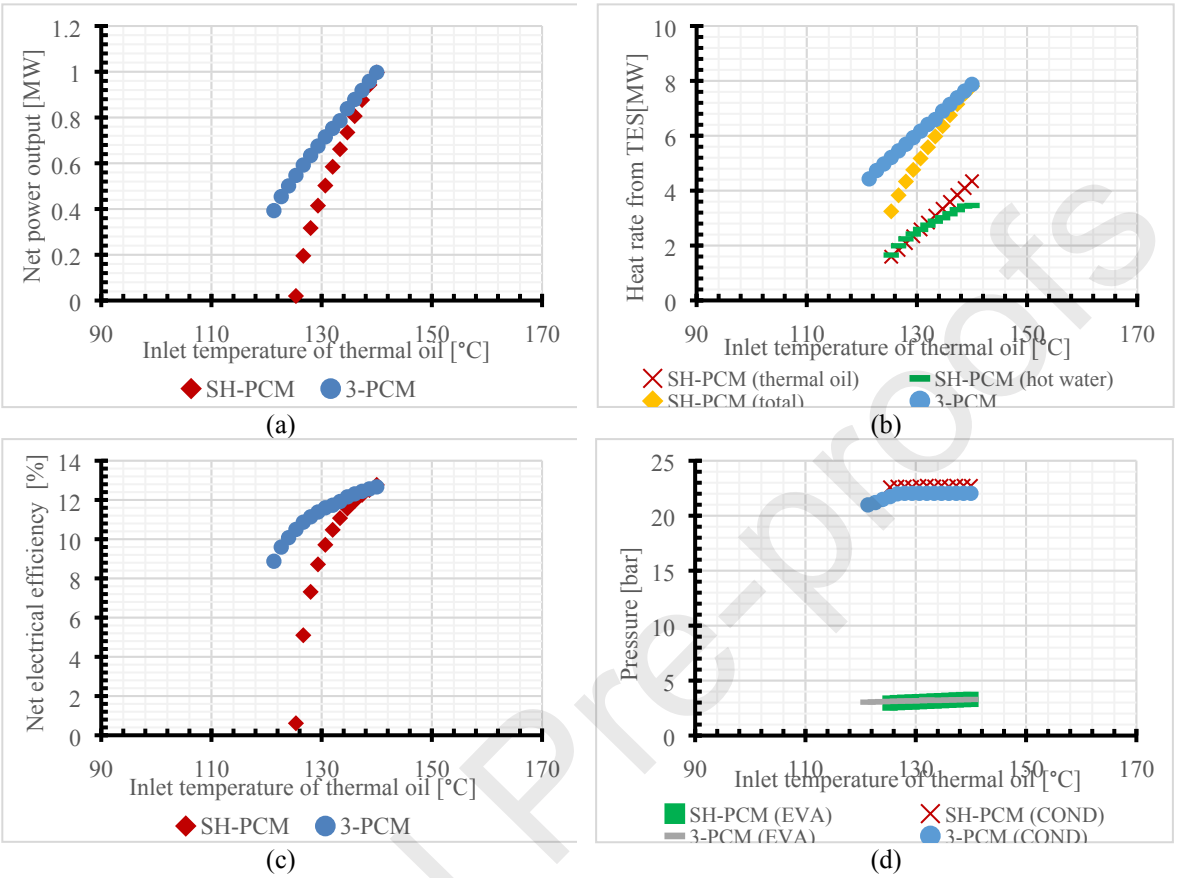

Fig. 8. Part-load optimization of ORC unit – Net electrical power output (a), heat rate from TES (b), net electrical efficiency (c) and evaporation and condensation pressures (d) for baseline SH-PCM case and cascaded PCM case (3-PCM).

Also, in the 3-PCM case study, it is required to reduce the mass flow rate of the working fluid in order to keep the outlet temperature of the thermal oil (the only heat source here) at the design value. However, only the outlet temperature of the thermal oil is fixed, while the temperature of the thermal oil at the end of preheating / beginning of the evaporation (pinch-point) is free to vary. This is a crucial difference with respect to the SH-PCM case. If the mass flow rate of working fluid is high, the thermal oil will be cooled down to a lower temperature at the pinch-point than in the SH-PCM case, and this would cause the temperature difference between the thermal oil and the working fluid in the preheating part to drop (for the same evaporation temperature). The drop in temperature difference corresponds to a drop in heat transfer rate in the preheating section and, therefore, the outlet temperature of the thermal oil can stay approximately constant and avoid dropping significantly. The overall result is that a larger mass flow rate of working fluid is allowed for a fixed outlet temperature of the thermal oil in the 3-PCM case compared with the SH-PCM. This results in a larger $\dot{W}_{net,ORC}$.

It can be seen in Fig. 8d that the evaporation and condensation pressures are kept close to their design value at part-load, so that a fixed pressure control strategy is used for both case studies. This control strategy is here thermodynamically advantageous on the hot side because of the constraint on the return temperature of the thermal oil, which is fixed to the design value. In this way, the evaporation temperature of the working fluid is always at the maximum allowed value (corresponding to the design evaporation pressure, which is the maximum allowed) and at the closest to the thermal oil temperature across the evaporator, thus

minimizing the temperature difference between thermal oil and working fluid. In the 3-PCM system, the evaporation pressure starts dropping for a thermal oil inlet temperature below 127 °C. This is required to ensure a positive degree of superheating at the turbine inlet for lower thermal oil inlet temperatures. The condensation pressure is hardly affected by the inlet temperature of the thermal oil and drops only slightly from 3.3 bar to 3.1 bar across the range of variation of the thermal oil inlet temperature.

4.1.2. Heat pump

The design of the HTHP was carried out following the description in Section 3.3. The optimum design variables for the SH-PCM and cascaded PCM cases are summarized in Table 14. The evaporation and condensation temperatures are approximately the same for both case studies (75 and 139 °C, respectively). These values are selected by the optimization routine to allow for maximum COP without incurring in temperature crossing in the condenser and evaporator. It can also be seen that it is thermodynamically favorable to minimize the pinch-point temperature differences in the evaporator and condenser, which are set to the minimum of 5 K. The major difference in the design conditions between the two case studies can be found in the normalized specific enthalpy at condenser outlet, which is lower for the 3-PCM case (-1.32 vs – 1.04). This allows for a lower mass flow rate of working fluid and therefore lower power consumed by the compressor (0.60 vs 0.65 MW_e). The considerably higher COP of the cascaded PCM case study can be explained by looking at the T-s diagrams at design conditions in Fig. 9. The temperature difference between the working fluid and the heat sink (hot water) in the subcooling section is much larger for the SH-PCM case study. This corresponds to high exergy destruction via heat transfer and, hence, to a lower COP. Indeed, the SH-PCM has room for improvement. For example, a more complex arrangement of the heat source and heat sink could be chosen to avoid that the heat sink (hot water) is partly at lower temperature that the heat source, which is thermodynamically unfavorable. Additionally, one could choose to fully charge the thermal oil before the hot water storage. This and further possible improvements are, however, out of the scope of the present work.

Table 14. Optimum design variables for HTHP unit.

Parameters	**SH-PCM**	**3-PCM**	**Unit**
Evaporation temperature	74.9	75.0	*°C*
Normalized specific enthalpy at condenser outlet	-0.99	-1.32	-
Normalized specific enthalpy at evaporator outlet	1.04	1.04	-
Pinch-point temperature difference at evaporator	5.0	5.0	*K*
Pinch-point temperature difference at condenser	5.2	5.0	*K*
Condensation temperature	139.1	139.2	*°C*
Mass flow rate of heat sink (thermal oil)	24.44	23.62	*kg/s*
Mass flow rate of heat sink (hot water)	2.85	-	*kg/s*
Mass flow rate of working fluid	9.8	9.1	*kg/s*
Isentropic efficiency of compressor	80.0	80.0	*%*
Compressor power input	0.65	0.60	MW_e
Coefficient of performance (COP)	3.84	4.36	-

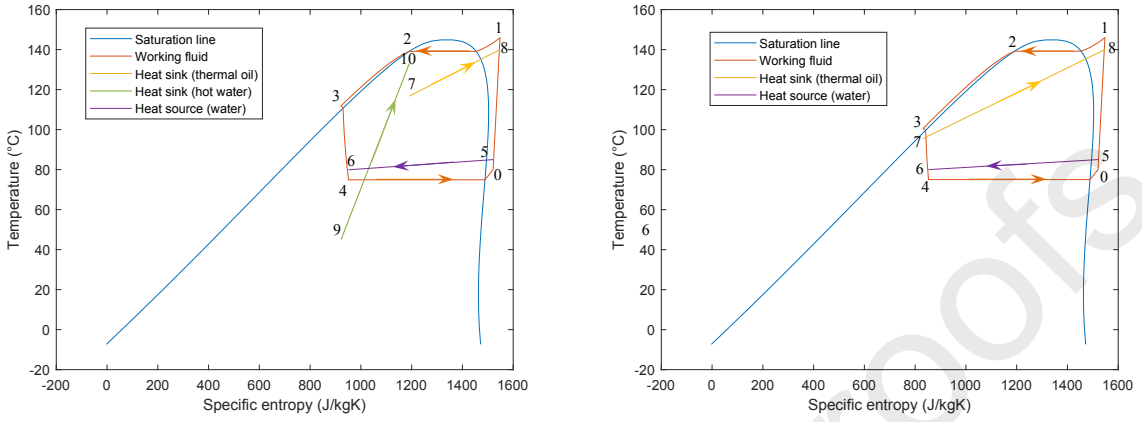

Fig. 9. T-s diagram of HTHP design conditions – (a) baseline SH-PCM case and (b) cascaded PCM case.

Following the same procedure as for the ORC unit, the results of the thermodynamic design routine were used to design the heat exchangers of the HTHP in Aspen EDR. After this, the part-load behaviour of the heat exchangers was simulated, and exponential functions were fitted to approximate the part-load performance. The heat transfer coefficients and part-load exponents derived from the fitting are reported in Table 15 and Table 16. The two cases mainly distinguish themselves for the presence of the hot water subcooler for the SH-PCM case, whereas the heat transfer coefficients and exponents for the evaporator and the condenser are the same for both cases, thanks to the very similar operating conditions. Both the design and the part-load performance data of the HTHP are in good agreement with the COP range provided in Ref. [19] for a heat source temperature of 85 ºC.

Table 15. Heat exchanger parameters of HTHP (SH-PCM case).

Heat exchanger	**Phase**	**Heat transfer area,** m^2	**Overall heat transfer coefficient,** W/m^2K	**Part-load parameter**	**Part-load exponent, -**
Condenser (thermal oil)	Liquid	0.0	184.8	$\dot{m}_{wf}$	0.7
	Two-phase	197.7	455.3	$\dot{m}_{wf}$	0.2
	Vapour	256.7	280.1	$\dot{m}_{oil}$	0.68
	Total	454.4	-	-	-
Subcooler (hot water)	Liquid	53.9	788.8	$\dot{m}_{wf}$	0.4
	Two-phase	-	-	-	-
	Vapour	-	-	-	-
	Total	53.9	-	-	-
Evaporator	Liquid	-	-	-	-
	Two-phase	204.7	1247.3	$\dot{m}_{wf}$	0.2
	Vapour	20.8	741.1	$\dot{m}_{wf}$	0.4
	Total	225.5	-	-	-

Table 16. Heat exchanger parameters of HTHP (3-PCM case).

Heat exchanger	Phase	Heat transfer area, m^2	Overall heat transfer coefficient, W/m^2K	Part-load parameter	Part-load exponent, -
Condenser (thermal oil)	Liquid	612.7	184.8	$\dot{m}_{wf}$	0.7
	Two-phase	185.4	455.3	$\dot{m}_{wf}$	0.2
	Vapour	226.0	280.1	$\dot{m}_{oil}$	0.68
	Total	1024.1	-	-	-
Evaporator	Liquid	0.0	-	-	-
	Two-phase	226.9	1247.3	$\dot{m}_{wf}$	0.2
	Vapour	18.9	741.1	$\dot{m}_{wf}$	0.4
	Total	245.8	-	-	-

During the charge phase, the thermal oil is heated up by the HTHP up to 140 ºC and then cooled down by the PCM storage. As the state of charge of the PCM storage increases, so does its temperature. Because of this, the return temperature of the thermal oil leaving the PCM storage and heading towards the HTHP increases, causing the HTHP to work at off-design conditions. The optimized part-load operation of the HTHP unit as a function of the inlet temperature of the thermal oil is depicted in Fig. 10 for the SH-PCM and the 3-PCM case studies. In both case studies, the power required to the compressor drops as the inlet temperature of the thermal oil increases. This is because a lower power is required to heat the thermal oil up to the fixed outlet temperature of 140 °C. The part-load performance of the HTHP units can be investigated by looking at their coefficient of performance. In this case, the behavior of the HTHP is very different. In the SH-PCM case study, the COP increases from 3.85 to 4.24 (10 %) when the inlet temperature of the thermal oil increases from 116 ºC to 126 ºC, before dropping back from 4.24 to 3.85 when the inlet temperature of the thermal oil increases from 126 ºC to 131 ºC. The reason for this is given by the fact that, although the inlet temperature of the thermal oil is increasing, the hot water also acts as a heat sink for the HTHP. The mass flow rate of the hot water from the sensible heat TES is modulated such that the ratio of the sensible to latent heat is kept analogous to the operation of the ORC unit. In this way, the thermal energy stored in the PCM and sensible heat TES could balance the thermal energy used during discharge. In the 3-PCM case, the thermal oil is the only heat sink for the HTHP. The increasing inlet temperature of thermal oil causes the HTHP to work far away from the design conditions and therefore the COP drops from 4.3 to 2.3 (by 53 %) when the inlet temperature of the thermal oil increases from 95.5 ºC to 130 ºC. The trends of the evaporation pressure and the condensation pressure are very similar for both case studies. The evaporation pressure varies between 11.0 and 12.0 bar between the minimum and the maximum of variation of the inlet temperature of the thermal oil. The condensation pressure, instead, is kept approximately to the design value of 36 bar for both cases.

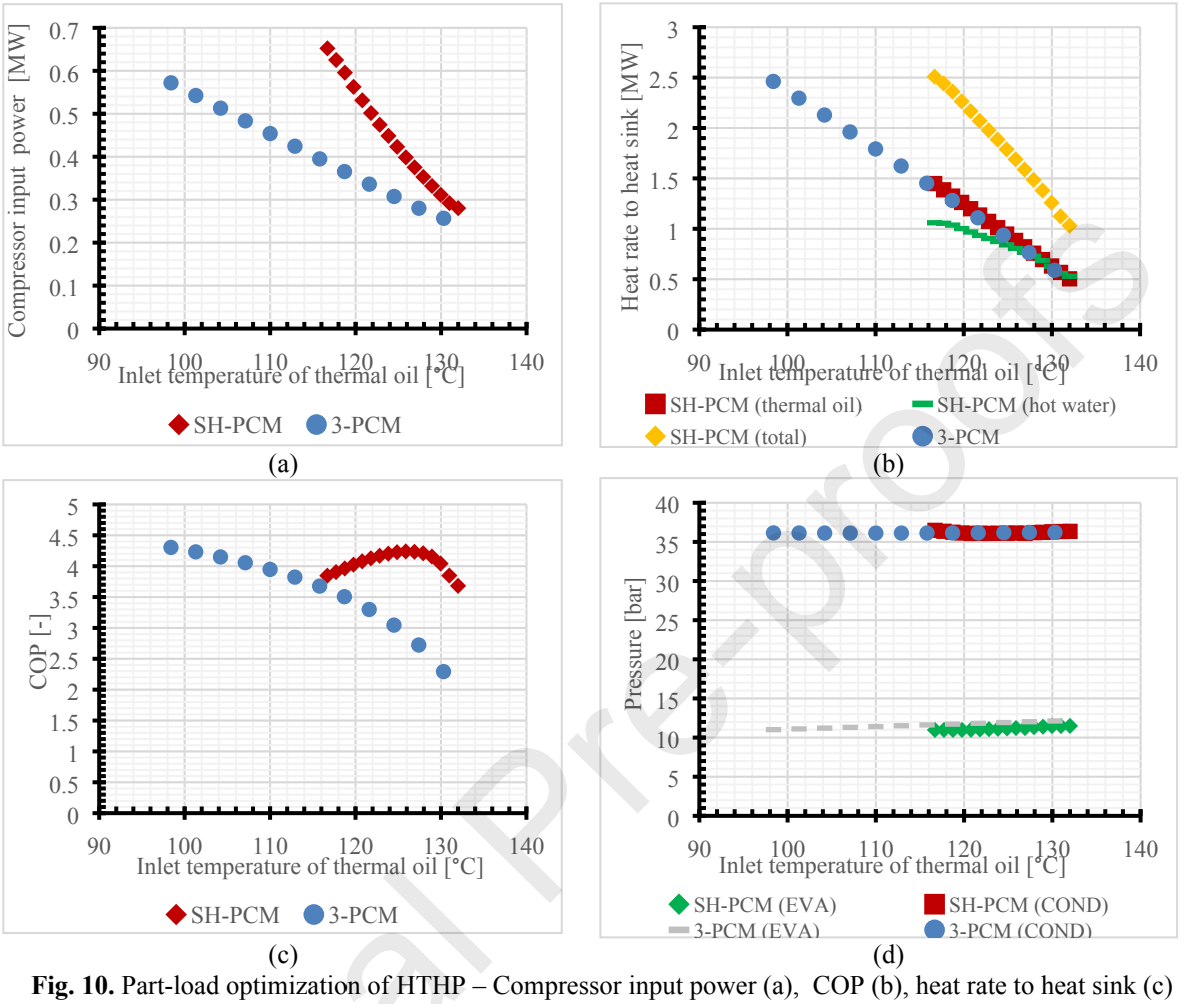

Fig. 10. Part-load optimization of HTHP – Compressor input power (a), COP (b), heat rate to heat sink (c) and evaporation and condensation pressures (d) for baseline SH-PCM case and cascaded PCM case (3-PCM).

4.2. Global performance analysis

Assuming the technical input data shown in Section 3 and the part-load performances of the HTHP and the ORC units, the two different scenarios corresponding to two different CHEST configurations were assessed. The effect of the different TES configuration over the CHEST performance has been summarized in Fig. 11. The implementation of the PCMs cascade solution allows approximately 100 % larger energy density of the system. In addition, the novel configuration significantly increases both the HTHP coefficient of performance and the ORC net electric efficiency, in turn enhancing the global performance of the system by 13 %. The reasons behind the thermodynamic superiority of the novel configuration can be explained as follows.

Fig. 12a reports the dynamic behaviour of the HTF temperature at the outlet of the TES during the CHEST discharge phase for the different configurations. Due to the thermocline phenomena approaching the outlet section of the TES during the discharge phase, where the HTF is heated up by the thermal energy stored by the particles, the temperature of the HTF at the outlet of the TES decreases over the time. Since this temperature corresponds to the inlet temperature of the HTF in the ORC evaporator, a decrease of the

instantaneous ORC net electric efficiency occurs over the time resulting in a lower round trip efficiency due to the part-load performance of the ORC unit. For a temperature of the HTF below the cut-off point, the ORC unit stops the operation.

The decrease of HTF outlet temperature over time is mitigated by the presence of the cascaded phase change process. Indeed, in the 3-PCM configuration, the TES system is capable to deliver thermal energy at higher temperature than the SH-PCM configuration resulting in a higher ORC net electric efficiency as shown in Fig. 12b. In fact, the PCM layers are not only capable to increase the total energy density (with respect to SH-PCM configuration), but also act as thermal "buffer" by keeping the outflow temperature within the cut-off temperature threshold for a longer time. Indeed, the phase change temperature transition allows the system to discharge for a longer period before the cut-off criterion is prompted. Therefore, there is an increase in the operating time (since the processes can continue while the outflow HTF temperature remains within these ranges), and thus in the amount of thermal energy which can be effectively withdrawn, resulting in a high efficiency in the use of the total storage capacity and a time averaged higher HTF temperature at the inlet of the ORC evaporator.

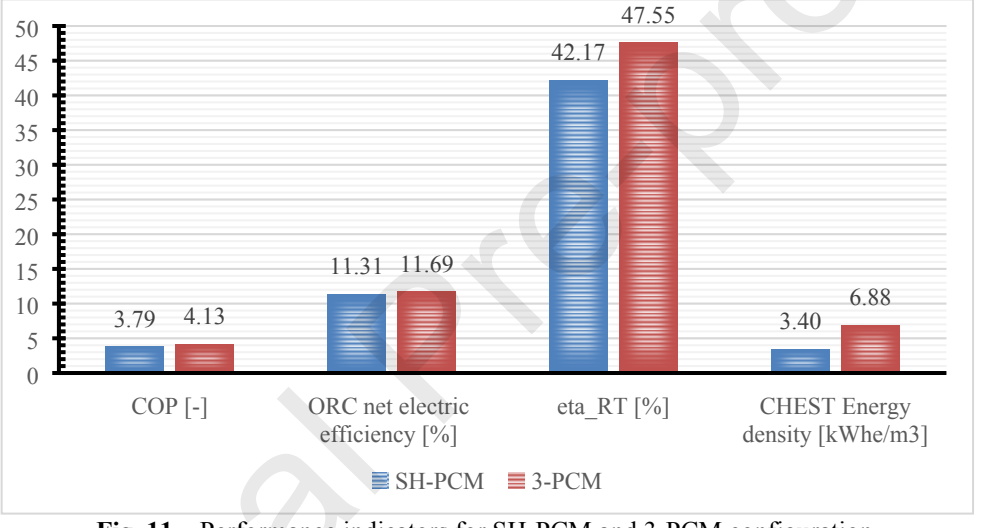

Fig. 11. Performance indicators for SH-PCM and 3-PCM configuration.

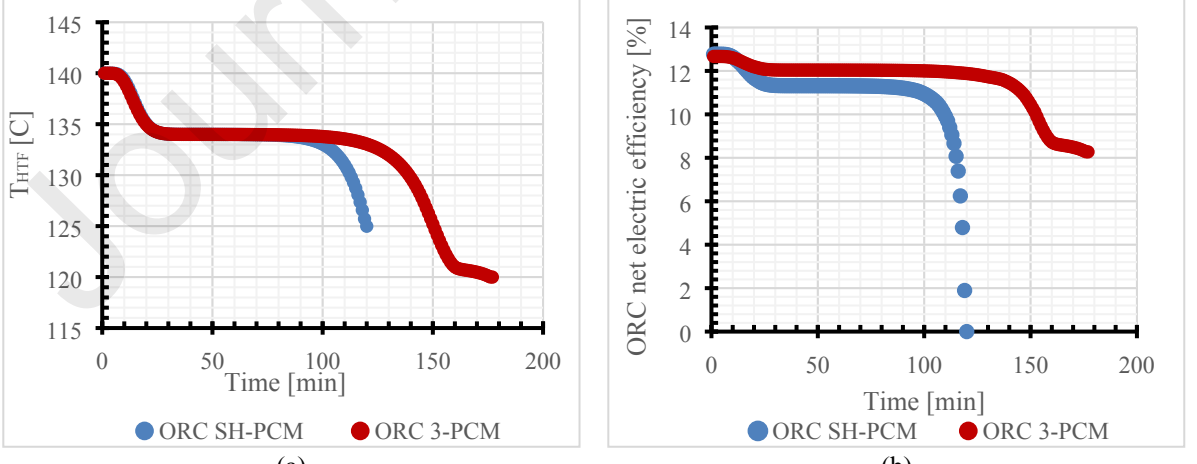

Fig. 12. Dynamic behaviour of HTF temperature at ORC inlet (a) and ORC net efficiency (b).

Similarly to what has been observed in the CHEST discharge phase involving the ORC-TES systems, the same "thermal buffer" effect is triggered also during the CHEST charge phase. Indeed, as shown in Fig. 13a, the increase of the HTF outlet temperature of the TES over time is mitigated by the presence of the cascaded phase change process of the PCM with the lowest phase change temperature (108 °C). This phenomenon allows to further stabilize the HTF temperature at the inlet of the HTHP at a lower value compared to the baseline scenario, achieving thus, according to the HTHP part-load behaviours shown in section 4.1.2, a higher COP (4.13 vs 3.79).

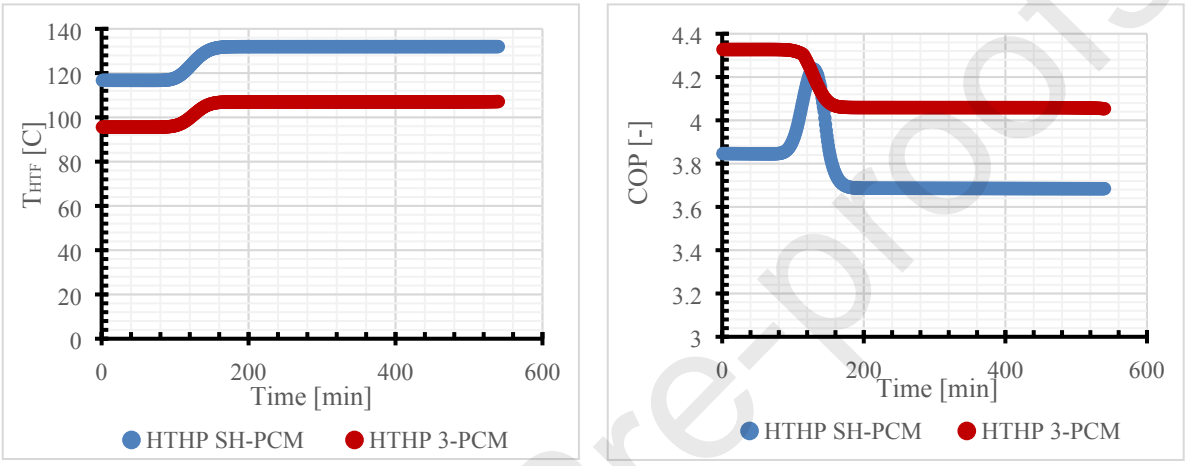

(a) (b)

Fig. 13. Dynamic behaviour of HTF temperature at HP inlet (a) and HP Coefficient of Performance (b).

5. Conclusions

Thermal energy storage was proved to be a crucial component for a compressed heat energy storage system, guaranteeing optimal operation and ensuring significantly high round trip efficiencies. Differently from the cascaded TES solution proposed in literature, the current work proposes and numerically investigate a novel CHEST configuration based on a cascaded phase change materials thermal energy storage. Furthermore, to the best of authors' knowledge, no literature study proposed a comprehensive and systematic analysis of the CHEST considering the dynamic behaviour of each component (high temperature heat pump, organic Rankine cycle and thermal energy storage). Conversely, this work developed for the first time a dynamic numerical model of the overall CHEST system in MATLAB in order to assess the potential thermodynamic advantage of a novel solution over the baseline scenario, currently proposed in literature. Once the models were validated guaranteeing a good level of confidence, the part-load behavior of the different CHEST configurations and their main components have been comparatively analyzed.

The technical study showed that the implementation of a cascaded PCM configuration significantly enhanced not only the CHEST energy storage density by 100 % but also the performance of the CHEST system. Indeed, by leveraging on the positive effect of the thermal buffer triggered by the cascaded PCM, the thermal energy storage is capable to: 1) achieve a better matching with the heat transfer fluid, leading to a better part-load performance of the ORC unit (11.69 % vs 11.31 %); 2) stabilize the thermal power delivered to the ORC evaporator enhancing thus the total electricity production of the discharge phase (2.19 vs 1.38 MWh_e) and 3) due to the presence of the PCM with the lowest phase change temperature at 108 °C, utilize more efficiently the heat sink, improving thus the COP of the charge phase by 9 % (4.13 vs 3.79).

The combined effect of both phenomena triggers a global performance enhancement of the cascaded configuration increasing the round trip efficiency by 13 % (47.6 % vs 42.2 %).

Any technical investigation presents well-defined boundaries of applicability due to the applied hypothesis and approximations. Therefore, it is paramount identifying the main limitations of the current study to fully comprehend the outcomes as well as identify potential areas for further improvements:

1) The optimization of the organic Rankine cycle, thermal energy storage and high temperature heat pump has been carried out sequentially. A global optimum might require iteration among the design phases, or an integrated global optimization routine could be developed.

2) Although a preliminary screening of potential PCMs and working fluids for thermal energy storage, organic Rankine cycle and high temperature heat pump has been carried out, a more systematic and comprehensive selection procedure could be applied.

3) Since high temperature heat pump technologies with heat sink temperature higher than 90 ºC are mostly under development only at a demonstration level, some uncertainties regarding the accuracy of the correlation for the compressor's isentropic efficiency can be identified and might be encompassed in the future once an adequate technological maturity will be achieved.

4) As a final remark, a comprehensive exergetic and economic analysis can be carried out in order to verify the economic performance of the novel CHEST configuration and further confirm its technological viability compared to the baseline scenario.

References

[1] IRENA. World energy transitions outlook. Irena 2022:1–20.

[2] Cozzi L, Gould T. World Energy Outlook 2021. IEA Publ 2021:1–386.

[3] Chen H, Cong TN, Yang W, Tan C, Li Y, Ding Y. Progress in electrical energy storage system: A critical review. Prog Nat Sci 2009;19:291–312. https://doi.org/10.1016/j.pnsc.2008.07.014.

[4] Luo X, Wang J, Dooner M, Clarke J. Overview of current development in electrical energy storage technologies and the application potential in power system operation q. Appl Energy 2015;137:511–36. https://doi.org/10.1016/j.apenergy.2014.09.081.

[5] Borri E, Tafone A, Romagnoli A, Comodi G. A review on liquid air energy storage: History, state of the art and recent developments. Renew Sustain Energy Rev 2021;137:110572. https://doi.org/10.1016/j.rser.2020.110572.

[6] Budt M, Wolf D, Span R, Yan J. A review on compressed air energy storage: Basic principles, past milestones and recent developments. Appl Energy 2016;170:250–68. https://doi.org/10.1016/j.apenergy.2016.02.108.

[7] Important MILESTONE: Status of the CHEST development and experiments » CHESTER Project n.d. https://www.chester-project.eu/news/status-of-the-chest-technology-and-experiments/ (accessed August 3, 2022).

[8] Abarr M, Geels B, Hertzberg J, Montoya LD. Pumped thermal energy storage and bottoming system part A: Concept and model. Energy 2017;120:320–31. https://doi.org/10.1016/j.energy.2016.11.089.

[9] Olympios A V, McTigue JD, Farres-Antunez P, Tafone A, Romagnoli A, Li Y, et al. Progress and prospects of thermo-mechanical energy storage—a critical review. Prog Energy 2021;3:022001. https://doi.org/10.1088/2516-1083/abdbba.

[10] Dumont O, Frate GF, Pillai A, Lecompte S, De paepe M, Lemort V. Carnot battery technology: A state-of-the-art review. J Energy Storage 2020;32. https://doi.org/10.1016/j.est.2020.101756.

[11] Steinmann WD. The CHEST (Compressed Heat Energy STorage) concept for facility scale thermo mechanical energy storage. Energy 2014;69:543–52. https://doi.org/10.1016/j.energy.2014.03.049.

[12] CHESTER Project n.d. https://www.chester-project.eu/ (accessed June 15, 2022).

[13] Steinmann WD, Jockenhöfer H, Bauer D. Thermodynamic Analysis of High-Temperature Carnot

Battery Concepts. Energy Technol 2020;8. https://doi.org/10.1002/ente.201900895.
[14] Roskosch D, Venzik V, Atakan B. Potential analysis of pumped heat electricity storages regarding thermodynamic efficiency. Renew Energy 2020;147:2865–73. https://doi.org/10.1016/j.renene.2018.09.023.
[15] Thess A. Thermodynamic efficiency of pumped heat electricity storage. Phys Rev Lett 2013;111:1–5. https://doi.org/10.1103/PhysRevLett.111.110602.
[16] Jockenhöfer H, Steinmann WD, Bauer D. Detailed numerical investigation of a pumped thermal energy storage with low temperature heat integration. Energy 2018;145:665–76. https://doi.org/10.1016/j.energy.2017.12.087.
[17] Sánchez-Canales V, Payá J, Corberán JM, Hassan AH. Dynamic modelling and techno-economic assessment of a compressed heat energy storage system: Application in a 26-MW wind farm in Spain. Energies 2020;13. https://doi.org/10.3390/en13184739.
[18] Hassan AH, O'Donoghue L, Sánchez-Canales V, Corberán JM, Payá J, Jockenhöfer H. Thermodynamic analysis of high-temperature pumped thermal energy storage systems: Refrigerant selection, performance and limitations. Energy Reports 2020;6:147–59. https://doi.org/10.1016/j.egyr.2020.05.010.
[19] Hassan AH, Corberán JM, Ramirez M, Trebilcock-Kelly F, Payá J. A high-temperature heat pump for compressed heat energy storage applications: Design, modeling, and performance. Energy Reports 2022;8:10833–48. https://doi.org/10.1016/J.EGYR.2022.08.201.
[20] Trebilcock F, Ramirez M, Pascual C, Weller T, Lecompte S, Hassan AH. Development of a compressed heat energy storage system prototype. Refrig Sci Technol 2020;2020-July:400–9. https://doi.org/10.18462/iir.rankine.2020.1178.
[21] Steinmann WD, Bauer D, Jockenhöfer H, Johnson M. Pumped thermal energy storage (PTES) as smart sector-coupling technology for heat and electricity. Energy 2019;183:185–90. https://doi.org/10.1016/j.energy.2019.06.058.
[22] Farid MM, Khudhair AM, Razack SAK, Al-Hallaj S. A review on phase change energy storage: Materials and applications. Energy Convers Manag 2004;45:1597–615. https://doi.org/10.1016/j.enconman.2003.09.015.
[23] Tafone A, Borri E, Cabeza LF, Romagnoli A. Innovative cryogenic Phase Change Material (PCM) based cold thermal energy storage for Liquid Air Energy Storage (LAES) – Numerical dynamic modelling and experimental study of a packed bed unit. Appl Energy 2021;301:117417. https://doi.org/10.1016/J.APENERGY.2021.117417.
[24] Wakao N. Effect of fluid dispersion coefficients on particle-to-fluid heat transfer coefficients in packed beds: Correlation of nusselt numbers. Chem Eng Sci 1979;34:325–36.
[25] Zanganeh G, Commerford M, Haselbacher A, Pedretti A, Steinfeld A. Stabilization of the outflow temperature of a packed-bed thermal energy storage by combining rocks with phase change materials. Appl Therm Eng 2014;70:316–20. https://doi.org/10.1016/j.applthermaleng.2014.05.020.
[26] Mertens N, Alobaid F, Frigge L, Epple B. Dynamic simulation of integrated rock-bed thermocline storage for concentrated solar power. Sol Energy 2014;110:830–42. https://doi.org/10.1016/j.solener.2014.10.021.
[27] Pili R, Romagnoli A, Jiménez-Arreola M, Spliethoff H, Wieland C. Simulation of Organic Rankine Cycle – Quasi-steady state vs dynamic approach for optimal economic performance. Energy 2019;167:619–40. https://doi.org/10.1016/J.ENERGY.2018.10.166.
[28] Pili R, Spliethoff H. Design and Off-Design of Organic Rankine Cycle Systems Recovering Fluctuating Industrial Waste Heat n.d.
[29] Organic Rankine Cycle (ORC) Power Systems. Org Rank Cycle Power Syst 2017. https://doi.org/10.1016/C2014-0-04239-6.
[30] Pili R, Bojer Jørgensen S, Haglind F. Multi-objective optimization of organic Rankine cycle systems considering their dynamic performance. Energy 2022;246:123345. https://doi.org/10.1016/J.ENERGY.2022.123345.

[31] REFPROP | NIST n.d. https://www.nist.gov/srd/refprop (accessed July 4, 2022).
[32] Constrained Nonlinear Optimization Algorithms - MATLAB & Simulink n.d. https://www.mathworks.com/help/optim/ug/constrained-nonlinear-optimization-algorithms.html#bsgppl4 (accessed December 12, 2022).
[33] Aspen Exchanger Design and Rating EDR | AspenTech n.d. https://www.aspentech.com/en/products/pages/aspen-exchanger-design-and-rating-edr (accessed July 4, 2022).
[34] Pili R, Siamisiis N, Agromayor R, Nord LO, Wieland C, Spliethoff H. Efficiency Correlations for Off-Design Performance Prediction of ORC Axial-Flow Turbines. 5 th Int. Semin. ORC Power Syst., 2019.
[35] Liu H, Zhao B, Zhang Z, Li H, Hu B, Wang RZ. Experimental validation of an advanced heat pump system with high-efficiency centrifugal compressor. Energy 2020;213:118968. https://doi.org/10.1016/J.ENERGY.2020.118968.
[36] Chen W, Xing Z, Tang H, Wu H. Theoretical and experimental investigation on the performance of screw refrigeration compressor under part-load conditions. Int J Refrig 2011;34:1141–50. https://doi.org/10.1016/J.IJREFRIG.2011.01.020.
[37] Song C, Gu M, Miao Z, Liu C, Xu J. Effect of fluid dryness and critical temperature on trans-critical organic Rankine cycle. Energy 2019;174:97–109. https://doi.org/10.1016/J.ENERGY.2019.02.171.

Highlights

- A CHEST system based on sensible heat and phase change material TES is investigated
- A dynamic approach of the CHEST system to assess the global performance is proposed.
- A novel TES configuration based on cascaded phase change materials is investigated.
- Cascaded concept is further enhanced to promote higher ORC and heat pump performances.
- Round trip efficiency's enhancement by 13 % is achieved implementing the novel system.

Declaration of interests

☒ The authors declare that they have no known competing financial interests or personal relationships that could have appeared to influence the work reported in this paper.

☐The authors declare the following financial interests/personal relationships which may be considered as potential competing interests: